

# Na<sub>3-x</sub>Er<sub>1-x</sub>Zr<sub>x</sub>Cl<sub>6</sub>—A Halide-Based Fast Sodium-Ion Conductor with Vacancy-Driven Ionic Transport

Roman Schlem, Ananya Banik, Mirco Eckardt, Mirijam Zobel, and Wolfgang G. Zeier\*


 Cite This: *ACS Appl. Energy Mater.* 2020, 3, 10164–10173


Read Online

ACCESS |



Metrics &amp; More



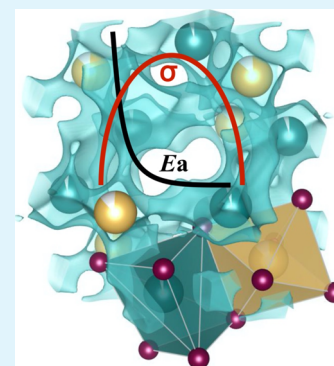
Article Recommendations



Supporting Information

**ABSTRACT:** Driven by the rising demand for consumer electronics, the field of all solid-state batteries employing solid electrolytes as the ion-conducting separator has attracted enormous attention in the last years. Recently, the lithium-conducting rare-earth halides A<sub>3</sub>MX<sub>6</sub> (A = Li, M = Y, Er, X = Cl, Br, I) and Li<sub>3</sub>InX<sub>6</sub> have been rediscovered as potential solid electrolytes, showing a good overall electrochemical performance, while the corresponding sodium-based compounds have been mostly overlooked yet. Here, we report the ionic transport properties of the Na-ion conducting rare-earth halide solid electrolyte Na<sub>3-x</sub>Er<sub>1-x</sub>Zr<sub>x</sub>Cl<sub>6</sub>. Na<sub>3-x</sub>Er<sub>1-x</sub>Zr<sub>x</sub>Cl<sub>6</sub> shows a conductivity enhancement from 10<sup>-9</sup> S·cm<sup>-1</sup> up to of ~0.04 mS·cm<sup>-1</sup> for Na<sub>2.4</sub>Er<sub>0.4</sub>Zr<sub>0.6</sub>Cl<sub>6</sub>, alongside interesting local structural rearrangements of the polyhedral motifs along the series of solid solutions. This series of halide-based sodium-ion conductors sheds light on promising compositions in search for superionic materials.

**KEYWORDS:** superionic conductor, sodium rare-earth halide, ionic conductivity, solid electrolyte, aliovalent substitution



## 1. INTRODUCTION

All solid-state batteries hold promise to meet the rising demand for high energy density and safe storage system over the conventional lithium-ion technology.<sup>1</sup> One major requirement is the use of highly conducting, electrochemically stable lithium ion conductors as a separator material and the conductive electrolyte in the cathode composites.<sup>2,3</sup> Although the performance of some solid electrolytes nearly match with the liquid counterparts,<sup>4–7</sup> challenges concerning interfacial decomposition reactions have not been solved yet.<sup>8–10</sup> Another potential issue with this Li-ion battery technology is the scarcity of the lithium metal, which further drives the search for an alternative.<sup>11</sup> Sodium can be used as an earth-abundant, low-cost substitute of lithium in the solid-state battery technology, provided the sodium-containing solid electrolytes can match the performance of their lithium counterparts.<sup>12</sup> Na<sub>3</sub>MS<sub>4</sub> (M = P/Sb),<sup>4,13–15</sup> Na<sub>11</sub>Sn<sub>2</sub>PS<sub>12</sub>,<sup>16–20</sup> and NaM<sub>2</sub>(PX<sub>4</sub>)<sub>3</sub> (M = Zr, Ti, X = O, S)<sup>21–25</sup> are well known names from this family. Recently, a high conductivity of up to 41 mS·cm<sup>-1</sup> has been realized for the tungsten-substituted Na<sub>3</sub>SbS<sub>4</sub>, resulting from a large concentration of Na-vacancies.<sup>4,26</sup> However, besides the needed high ionic conductivity, a chemical compatibility to the used electrodes, a high electrochemical stability, and general processing capabilities are needed.<sup>27–29</sup> Although a multitude of sodium-containing thiophosphates perform great with respect to conductivity, the limited voltage stability window hinders reaching high energy densities within the resulting batteries.<sup>30,31</sup> On the contrary, highly stable oxide super ionic conductors (e.g., NASICONs and β-alumina) that exhibit a

sufficient electrochemical window exhibit high grain boundary resistances and require harsh synthesis conditions.<sup>32</sup>

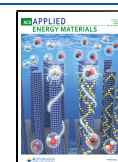
Recently, the rare-earth-containing halide compounds Li<sub>3</sub>MX<sub>6</sub> (M = Y, Er; X = Cl, Br, I) have attracted growing interest, as they combine the high ionic conductivity of thiophosphates up to the 1 mS·cm<sup>-1</sup> range and the large voltage stability window up to 4 V comparable to known oxides.<sup>33–39</sup> From the recent report of Wang *et al.*,<sup>40</sup> it is clear that the halide anionic framework is responsible for the low-ion migration energy barrier and high electrochemical stability in these materials. The monovalent nature of chloride leads to weaker interactions with the Li-ion and hence fast conducting ion diffusion pathways as compared to the sulfide electrolyte. Among these halides, the chlorides promise to be the best choice as the higher electronegativity of the chloride results in better oxidative stability,<sup>41</sup> which further drives the current exploration of the chloride-based electrolyte systems for solid-state battery application.

One possible approach to expand the use of these materials would be the search for Na-conducting ternary halide electrolytes.<sup>42,43</sup> In this paper, we report the successful synthesis of the novel Na<sub>3-x</sub>Er<sub>1-x</sub>Zr<sub>x</sub>Cl<sub>6</sub> substitution series (x

**Received:** August 4, 2020

**Accepted:** September 3, 2020

**Published:** September 3, 2020



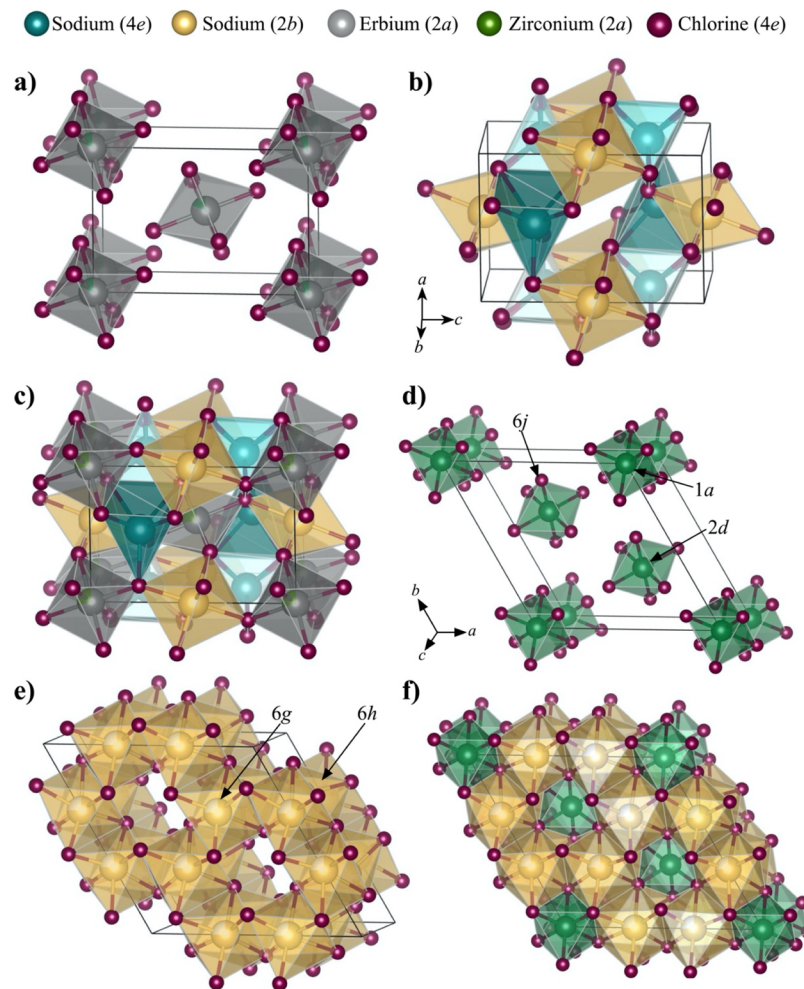


**Figure 1.**  $\text{Na}_3\text{ErCl}_6$  structure, (a) built up by a bcc-like arrangement of  $\text{ErCl}_6^{3-}$  octahedra. (b) Two different Na-polyhedra can be found that are either prisms or octahedra, being linked either by a corner or edge. The full structure is shown in (c).  $\text{Na}_2\text{ZrCl}_6$  structure, (d) built up by  $\text{ZrCl}_6^{2-}$  octahedra. (e) Na-octahedra build a honeycomb-like arrangement around the  $\text{ZrCl}_6^{2-}$  octahedra. The full structure is shown in (f). Unlike the  $\text{Na}_3\text{ErCl}_6$  structure, here, the polyhedra are either face- or edge-sharing.

= 0–1) *via* mechanochemical synthesis, where substitution of  $\text{Er}^{3+}$  by  $\text{Zr}^{4+}$  introduces sodium vacancies and provides necessary free lattice sites for ionic diffusion. Using a combination of powder X-ray diffraction and impedance spectroscopy, we explore the influence of the substitution on the structure, the  $\text{Na}^+$  concentration, and the ionic transport. Introduction of  $\text{Zr}^{4+}$  in the  $\text{Er}^{3+}$  site leads to changes in the local arrangement of the different polyhedral motifs, it increases the Na-ion vacancy concentration, which in turn improves the ionic conductivity and decreases the activation barriers for ionic motion. As a result of a successful vacancy incorporation and activation energy reduction, an ionic conductivity of  $\sim 0.04 \text{ mS}\cdot\text{cm}^{-1}$  is achieved for  $\text{Na}_{2.4}\text{Er}_{0.4}\text{Zr}_{0.6}\text{Cl}_6$ , which is four orders of magnitude higher than that of the pristine  $\text{Na}_3\text{ErCl}_6$ . This work provides a first framework for these new sodium–halide-based superionic conductors.

## 2. EXPERIMENTAL METHODS

**2.1. Synthesis.** All syntheses were carried out under Ar atmosphere. NaCl (Merck, 99.5%, pre-dried at 200 °C for 48 h under dynamic vacuum),  $\text{ErCl}_3$  (Sigma-Aldrich, 99%), and  $\text{ZrCl}_4$  (Alfa Aesar, 99.5%) were used as received. The syntheses were carried out using around 5–10 wt % excess of  $\text{ErCl}_3$  similarly as described

elsewhere for the synthesis of  $\text{Li}_3\text{ErCl}_6$ .<sup>35</sup> For the mechanochemical synthesis, the mixtures were put into 45 mL ball mill cups using a 30:1 mass ratio for 5 mm  $\text{ZrO}_2$  milling media: precursor powder. The reactions were carried out for a total of 99 cycles, with a cycle consisting of a milling time of 15 min at 500 rpm, followed by a rest step of 5 min. For the subsequent crystallization, the powder was put into predried ampoules and then placed into a preheated furnace for 5 min at 550 °C. To ensure a precise annealing time, the powder-containing ampoules were air-quenched.

**2.2. X-ray Diffraction and Structural Analyses.** X-ray diffraction was carried out with a STOE STADI P Mythen2 4K diffractometer (Ge(111) monochromator; Ag  $K\alpha_1$  radiation,  $\lambda = 0.5594 \text{ \AA}$ ) using four Dectris MYTHEN2 R 1K detectors in Debye–Scherrer geometry.<sup>44</sup> Scattering data were acquired over a  $q$ -range of  $0.3\text{--}20.5 \text{ \AA}^{-1}$  with a resolution of  $0.0029 \text{ \AA}^{-1}$  (based on 50  $\mu\text{m}$  strip width of MYTHEN2 R 1K modules and instrument geometry). All samples were sealed in glass capillaries (Hilgenberg,  $\varnothing = 0.5 \text{ mm}$ ) and measured for a total time of 22 h each, except samples with composition  $x = 0.7$  and 0.9, which were measured 8 h each.

Rietveld refinements were carried out using the TOPAS software package. Rietveld refinements included (1) background and scaling factor, (2) lattice parameters and peak shape, and (3) atomic positions and respective thermal displacement parameters. After refining the sodium occupancies (see Table S1 for constraints), all the parameters were opened up simultaneously to achieve the best possible fit. If this resulted in physically unreasonable values (high Na

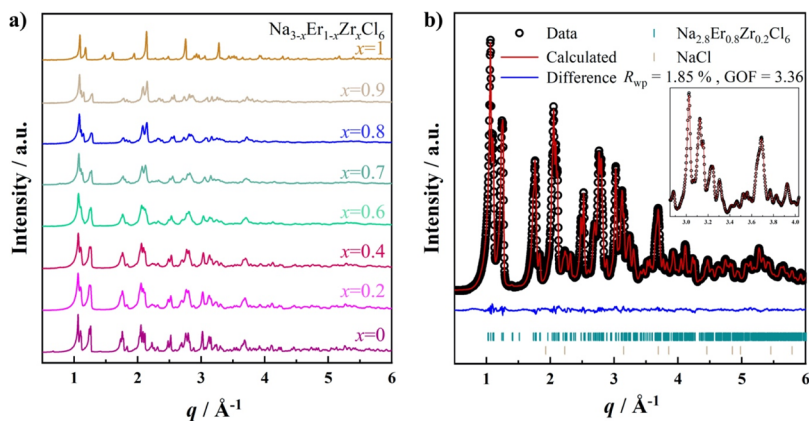


**Figure 2.** Comparison of all collected X-ray diffraction patterns (a) showing that the full substitution-series crystallizes in the  $P2_1/n$  space group except for  $\text{Na}_2\text{ZrCl}_6$  that crystallizes in the  $P\bar{3}m1$  space group, thereby having the same space group as  $\text{Li}_3\text{ErCl}_6$ . An exemplary Rietveld refinement (b) shows the good match of the refined data, with a low amount of NaCl impurity (2 wt %).

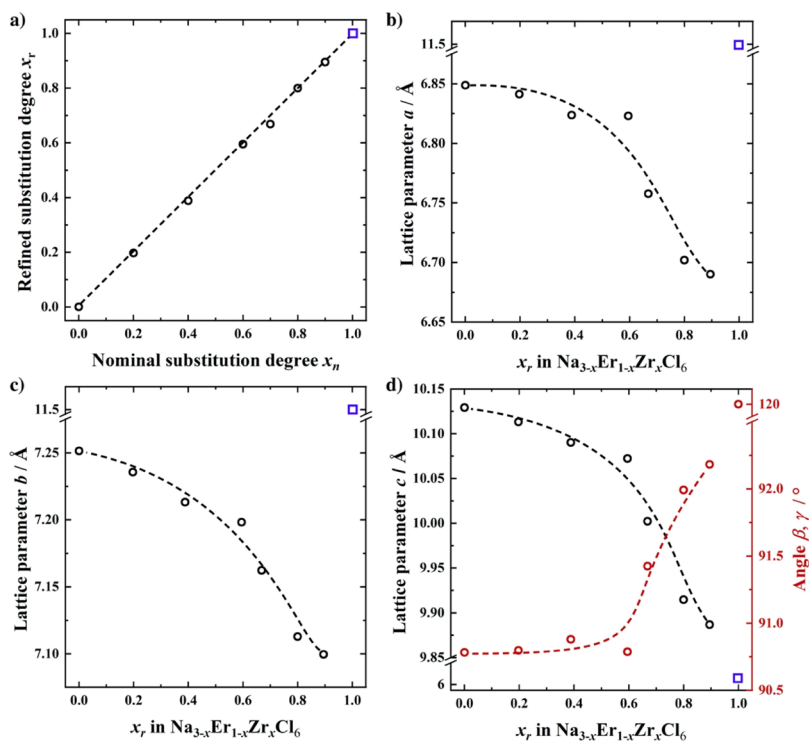


**Figure 3.** Refined  $\text{Zr}^{4+}$  content vs nominal  $\text{Zr}^{4+}$  content showing no visible solubility limit (a). Influence of the Zr substitution on the lattice parameters (b–d), as well as the angle (d). Dashed lines act as a guide to the eye, with the endmember  $x = 1$  ( $\text{Na}_2\text{ZrCl}_6$ ), being excluded for the lattice-related values as the compound crystallizes in a different space group. A decrease can be observed for the lattice parameters caused by the smaller ionic radius of  $\text{Zr}^{4+}$  in comparison to  $\text{Er}^{3+}$ . The angle appears to increase for large substitution degrees, changing toward the angle of  $\text{Na}_2\text{ZrCl}_6$  ( $120^\circ$ ).

thermal displacement), the values from the refinement before were taken as final values.

**2.3. Electrochemical Impedance Spectroscopy.** An impedance spectroscopy analysis was used to assess the ionic conductivities. The electrochemical impedance analysis was conducted in the temperature range of  $-40$  to  $50$   $^\circ\text{C}$ , with an equilibration time of 1 h per step using a VMP300 impedance analyzer in the frequency range of 7 MHz to 100 mHz. Roughly 200 mg of powder was filled into press cells that use steel stamps as current collectors.<sup>9</sup> The cells were pressed with a uniaxial pressure of 382 MPa for 3 min followed by a slow pressure-release step. The press cells were fixed in frames using a torque of 10 Nm for the measurements.

**2.4. Bond Valence Sum Analyses.** The bond valence sum (BVS) analysis was performed using the softBV software tool with a grid size of 0.1 Å. The obtained energy landscape was merged with the initially used structure file (CIF).<sup>45</sup> The BVS method is purely based on coulombic interaction and yields a possible diffusion pathway with minimal valence mismatch of the mobile ion. A detailed description of the BVS method can be found in ref 45.

### 3. RESULTS

**3.1. Structure of  $\text{Na}_3\text{ErCl}_6$  and  $\text{Na}_2\text{ZrCl}_6$ .** Although the Na analogue of the rare-earth chlorides,  $\text{Na}_3\text{MCl}_6$  ( $\text{M} = \text{La} - \text{Lu}$ ), have long been known, studies on their ionic transport properties are rare.<sup>46,47</sup>  $\text{Na}_3\text{ErCl}_6$  crystallizes in a distorted

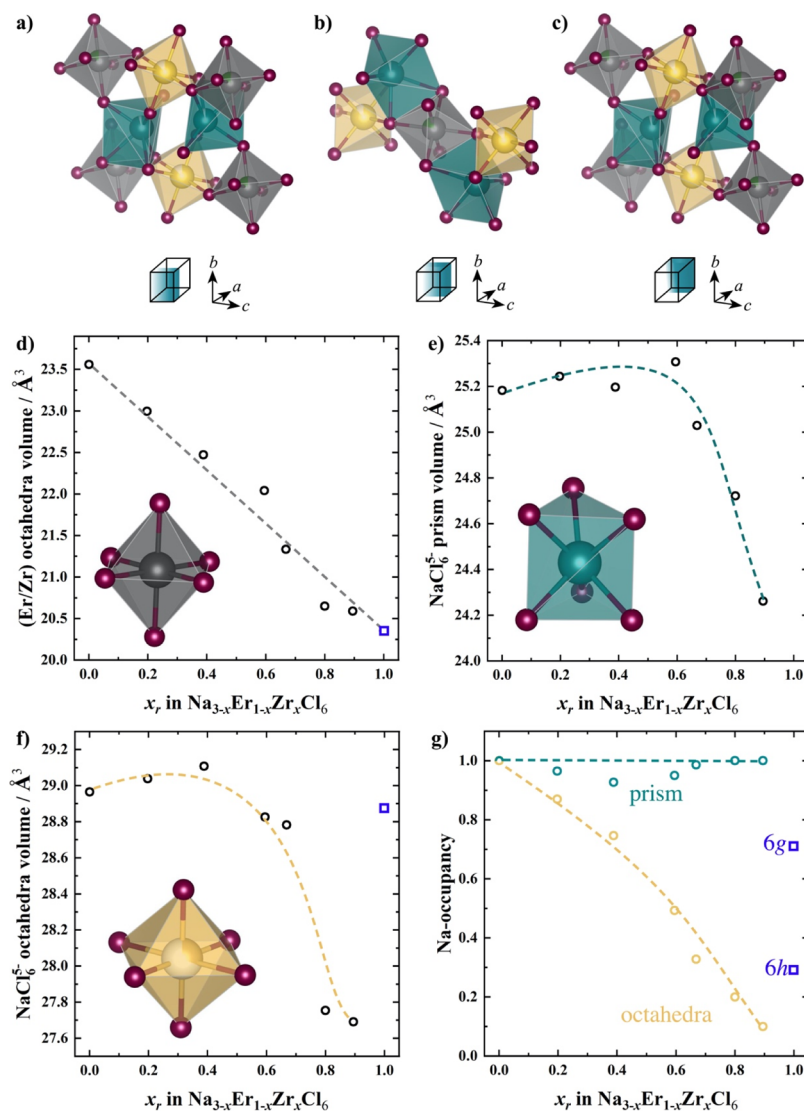


**Figure 4.** (a–c) Cuts through the unit cell of  $\text{Na}_3\text{ErCl}_6$  showing the highly interconnected  $\text{MCl}_6$  polyhedra. (d)  $(\text{Er}_{1-x}\text{Zr}_x)\text{Cl}_6^{(3-x)-}$  polyhedral volumes, which exhibit a linear decrease with increasing Zr content. (e,f) Na-prism and octahedra volumes and (g) Na-occupancies on both Na-Wyckoff positions. The Na-polyhedra sizes initially slightly increase, with a strong decrease after exceeding a substitution degree of  $x = 0.6$ , following the same trend as the decreasing lattice parameters. The constant Na-occupancy within the prism and steadily decreasing Na-occupancy within the octahedra is indicative for a higher stability of the prismatic coordination for sodium within this structure.

cryolite type structure with monoclinic space group ( $P2_1/n$ ).<sup>48</sup> The crystal structure of  $\text{Na}_3\text{ErCl}_6$  is shown in Figure 1 along different crystallographic orientations. The structure comprises an  $\text{ErCl}_6^{3-}$  octahedral framework located at the corners of the unit cell, as well as the body-centered position (0.5, 0.5, 0.5) with Er occupying the Wyckoff 2a position. The close resemblance of  $\text{Na}_3\text{ErCl}_6$  with a body-centered cubic (bcc) structure hints at a possible favorable ionic conduction process in this class of materials.<sup>49</sup> Sodium occupies two different crystallographic positions, which form octahedral (Wyckoff 2b) and prismatic (Wyckoff 4e) sites (Figure 1b) for the two different  $\text{NaCl}_6^{5-}$  polyhedra. Each  $\text{NaCl}_6^{5-}$  prism is connected by an edge or corner-sharing arrangement with another  $\text{NaCl}_6^{5-}$  octahedron. The full structure is displayed in Figure 1c, showing its dense polyhedral packing and complexity. The  $\text{ErCl}_6^{3-}$  polyhedra share edges with the  $\text{NaCl}_6^{5-}$  prism, indicating an influence of the Er polyhedra on the Na-diffusion pathway.

The pristine  $\text{Na}_3\text{ErCl}_6$  has only fully occupied sodium polyhedra, which are expected to result in poor ion conduction, as vacant adjacent sites are needed for the mobile species to jump to. Therefore, aliovalent substitution may be needed to improve the ion transport of  $\text{Na}_3\text{ErCl}_6$  via substitution of Er with higher valent cations, which hopefully tunes the Na-vacancy density along with diffusion pathway modification. In this work,  $\text{Zr}^{4+}$  ( $r = 72$  pm) was selected as a substituent for  $\text{Er}^{3+}$  ( $r = 89$  pm) because of its large ionic radius compared to other tetravalent metal ions.<sup>50</sup> However, unlike  $\text{Na}_3\text{ErCl}_6$ ,  $\text{Na}_2\text{ZrCl}_6$  crystallizes in the trigonal  $\bar{P}3m1$  space group, similar to  $\text{Li}_3\text{ErCl}_6$ .<sup>35,39</sup> In  $\text{Na}_2\text{ZrCl}_6$ , Zr resides in octahedrally coordinated Wyckoff 1a, 1b, and 2d positions. Na occupies octahedrally coordinated 6g and 6i Wyckoff positions, with a partial occupation for both the possible Na-octahedra, which build a honeycomb lattice in the  $ab$ -plane and every octahedron shares at least one edge with another octahedron. The honeycomb arrangement leads to favorable ionic transport

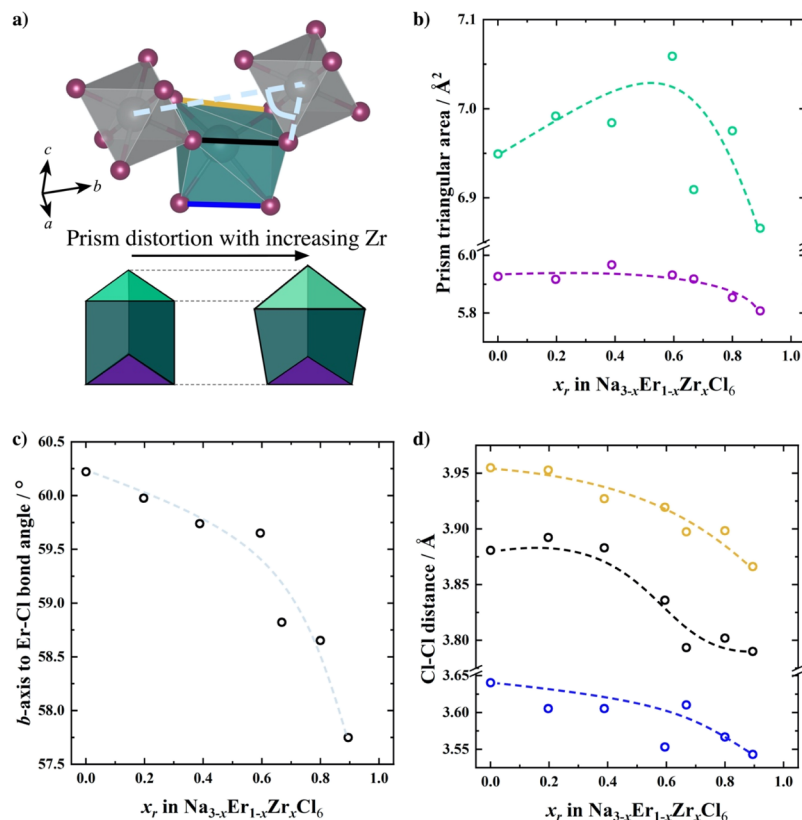


**Figure 5.** Structural excerpt and schematic prism transition-area distortion (a), with corresponding values in (b)—bottom area in purple and top area in light green. An Er-octahedra rotation can be expressed by the changing angle of the  $b$ -axis with an Er-Cl bond (c). The resulting prism distortion can be further shown by the changing edge lengths of the prism, colored black, yellow, and blue in (a), where all decrease with increasing Zr content (d). With the shrinking unit cell, the edge lengths of the prism decrease in size; however, the Er-octahedra rotation results in an expansion of the trigonal area and eventually the initial prism size increase, as discussed in Figure 4e.

at least in the lithium counterparts, as recently shown for  $\text{Li}_3\text{ErCl}_6$  and  $\text{Li}_3\text{YCl}_6$ .<sup>35,39,51</sup>

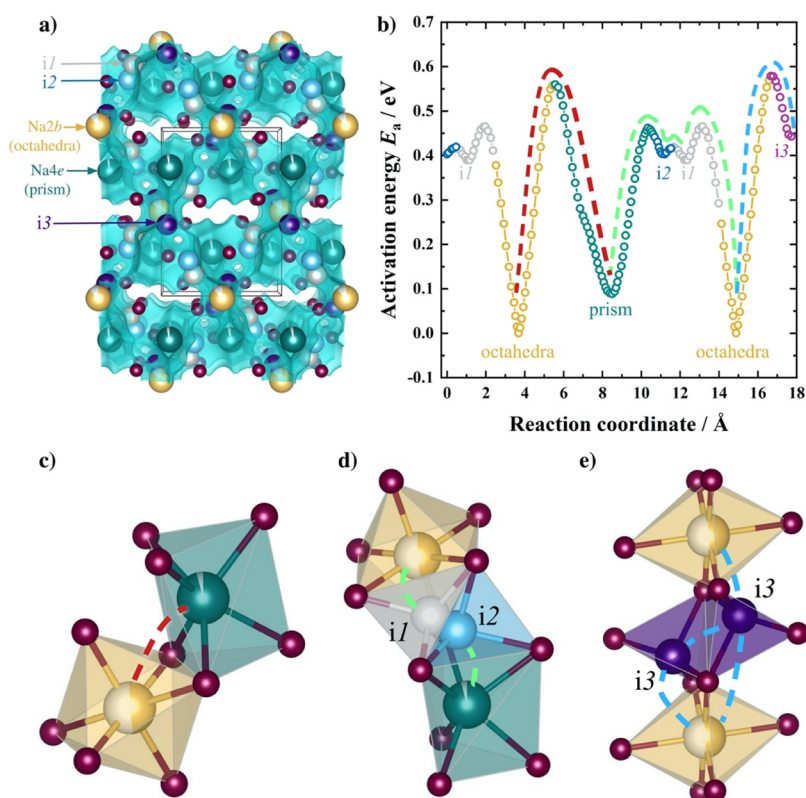
**3.2. General Structural Changes.** To study the influence of  $\text{Na}^+$  vacancy introduction associated with the  $\text{Zr}^{4+}$  substitution, in the crystal structure and ion transport, Zr-substituted  $\text{Na}_3\text{ErCl}_6$  samples are prepared with increasing Zr/Er ratio ( $\text{Na}_{3-x}\text{Er}_{1-x}\text{Zr}_x\text{Cl}_6$ ,  $x = 0-1$ ). Initially, a step size of 0.2 was used; however, the occurring structural changes above  $x > 0.6$  warranted smaller steps in the solid solutions of  $\Delta x = 0.1$ . Rietveld refinements against X-ray diffraction data were used to assess these structural changes. Figure 2 shows the summary of the collected X-ray diffraction data of all compositions and a representative Rietveld refinement. The diffraction patterns of  $\text{Na}_3\text{ErCl}_6$  and  $\text{Na}_2\text{ZrCl}_6$  confirm the monoclinic and trigonal crystal structure of the parent compounds, respectively. Upon incorporation of  $\text{Zr}^{4+}$ ,  $\text{Na}_{3-x}\text{Er}_{1-x}\text{Zr}_x\text{Cl}_6$  adopts the monoclinic crystal structure of the  $\text{Na}_3\text{ErCl}_6$  endmember. A minor phase fraction of a NaCl impurity is found, which is unlikely to affect the ionic transport properties (see Tables S2–S10 Supporting Information).<sup>52</sup> Low values for the fit residuals indicate a good match of the theoretical structure and measured data. The constraints and resulting fit parameters for every Rietveld refinement can be found in Supporting Information (Table S1).

Figure 3a shows the refined Zr content in  $\text{Na}_{3-x}\text{Er}_{1-x}\text{Zr}_x\text{Cl}_6$  against the nominal content. A linear behavior is observed corroborating the existence of solid solutions. Hereafter, all compositions are shown against the refined content of Zr,  $x_r$ . Figure 3b–d shows the evolution of the lattice parameters

upon Zr substitution in  $\text{Na}_3\text{ErCl}_6$ . All the lattice parameters decrease with increasing  $x$  in  $\text{Na}_{3-x}\text{Er}_{1-x}\text{Zr}_x\text{Cl}_6$  for  $x = 0-0.6$ , which is likely caused by the smaller ionic radius of  $\text{Zr}^{4+}$  (72 pm) in comparison to  $\text{Er}^{3+}$  (89 pm).<sup>50</sup> However, the change in the lattice parameters is not linear; for  $x \geq 0.6$ , a sharper reduction is observed for all the lattice parameters along with an increase in the unit cell angle. This sharp change in the behavior of the lattice may be related to underlying changes in the polyhedra, which needs to be explored.

**3.3. Polyhedral Changes.** To obtain further insights into the changing structural features, the M-polyhedra are of interest as they are highly interconnected and are likely directly influencing the resulting diffusion pathways and hence the transport properties.<sup>53,54</sup> The connection of the different polyhedra are shown in Figure 4a–c. Figure 4d shows the polyhedral volume of  $(\text{Er}_{1-x}\text{Zr}_x\text{Cl}_6)^{(3-x)-}$  as a function of the refined  $\text{Zr}^{4+}$  substitution. The absence of a solubility limit as discussed in Figure 3a and the complete incorporation of  $\text{Zr}^{4+}$  in the  $\text{Er}^{3+}$  site of the  $\text{Na}_{3-x}\text{Er}_{1-x}\text{Zr}_x\text{Cl}_6$  series is further supported by the linear dependence of the  $\text{MCl}_6$  octahedral volume. With increasing amount of the smaller  $\text{Zr}^{4+}$  on the  $\text{Er}^{3+}$  site, the octahedral volume decreases in a linear fashion. This is in particular interesting as the lattice parameters (*vide supra*) do not change linearly over the whole series of solid solutions, which warrants an investigation of the  $\text{Na}^+$  polyhedra.

With increasing  $\text{Zr}^+$  content, a slight increase of the  $\text{NaCl}_6^{5-}$  prismatic and octahedral volume can be seen until a substitution degree of  $x = 0.6$ , as shown in Figure 4e,f,



**Figure 6.** Lowest energy bond-valence landscape (a) showing the preferred sodium diffusion trajectory. Potential landscape of  $\text{Na}_{2.8}\text{Er}_{0.8}\text{Zr}_{0.2}\text{Cl}_6$  with three different diffusion mechanisms with colored pathways shown in (c–e), respectively [same colors red, green, and blue used in (b,c–e) for different pathways]. Direct octahedra–prism transition without involving any of the found interstitial positions (c), prism–octahedra transition *via* two tetrahedral interstitial sites (d), and octahedra–octahedra *via* the third interstitial site (e).

respectively. Exceeding a  $\text{Zr}^{4+}$  content of 60 %, both  $\text{Na}^+$  polyhedra decrease in volume following the general trend of the decreasing lattice parameters (Figure 3b–d). Figure 4g shows the Na occupancies on the two different Na positions. While the Na occupancy on the Wyckoff 4e position does not change significantly (prismatic  $\text{Na}^+$  polyhedron), the occupancy on the Wyckoff 2b position ( $\text{Na}^+$  octahedron) steadily decreases. Clearly the octahedral environment can stabilize vacancies, whereas empty sites seem to be unfavorable for the prismatic coordination environment here. Although the linear increase of  $\text{Zr}^{4+}$  in the structure alongside with a linear decrease of the  $(\text{Er}_{1-x}\text{Zr}_x\text{Cl}_6)^{(3-x)-}$  polyhedral volume is expected, the nonlinear trends of the lattice parameters and  $\text{Na}^+$ -polyhedral volumes suggest some interrelated compensation mechanism.

Here, three possible mechanisms may be related that influence the  $\text{NaCl}_6^{5-}$  polyhedra size: (1) the generally decreasing unit-cell volume should result in a decreasing polyhedra size, nevertheless an increasing polyhedral volume is observed at first. (2) The influence of the  $\text{Na}^+$  occupancy within the polyhedra cannot be neglected and should surely influence the resulting polyhedral size. However, the occupancy on the prismatic site does not change while the volume decreases ruling this influence out in parts. (3) The low symmetry space group allows for a slight rearrangement of the halide ions, possibly leading to slight distortions of the polyhedra that may change within the local structure. This distortion can be explored by investigating the local environment of the prisms, as shown in Figure 5b–d, with the corresponding distances and angles shown in the schematic

structure in Figure 5a. Figure 5c shows the distortion in the Er–Er–Cl angle along the *b*-axis as a function of the Zr amount. The Er–Er–Cl angle decreases with increasing substitution degree, indicating rotation of the  $\text{ErCl}_6^{3-}$  octahedra on the edges of the prism. As the  $\text{NaCl}_6^{5-}$  prism shares edges with those  $\text{ErCl}_6^{3-}$  octahedra, this rotation influences the prism size, as seen in Figure 4e. Figure 5d shows the distance of nearest neighboring chloride ions of two adjacent  $\text{ErCl}_6^{3-}$  polyhedra that are connected to a common  $\text{NaCl}_6^{5-}$  prism, as seen in Figure 5a. The decreasing Cl–Cl distances are indicative of the distortion of the prism associated with the observed  $(\text{Er}_{1-x}\text{Zr}_x\text{Cl}_6)^{(3-x)-}$  volume reduction (see Figure 4d). The impact of the rotation of the  $\text{ErCl}_6^{3-}$  octahedra can be further understood based on the trigonal transition areas of the  $\text{NaCl}_6^{5-}$  prism. The trigonal transition areas (marked in green and purple in Figure 5a,b), formed by the edge-shared chloride ions, increases significantly until a substitution degree of  $x = 0.6$  and thereby likely driving this increasing prism size.

Regarding all these different prism features, it is clear how strongly the low symmetry space group allows for a repositioning of the halide ions, resulting in this strong prism distortion that is indicated in Figure 5a. Overall, the changing composition that enforces changing occupancies and polyhedral volumes leads to local distortions of the different polyhedra that persist throughout the series of solid solution until the unit cell becomes too small to allow for the distortion, leading to a transition to the structure of  $\text{Na}_2\text{ZrCl}_6$ .

**3.4. Diffusion Pathways.** In addition to the observed changes in the  $\text{Na}^+$  polyhedra, a bond-valence-sum analysis was

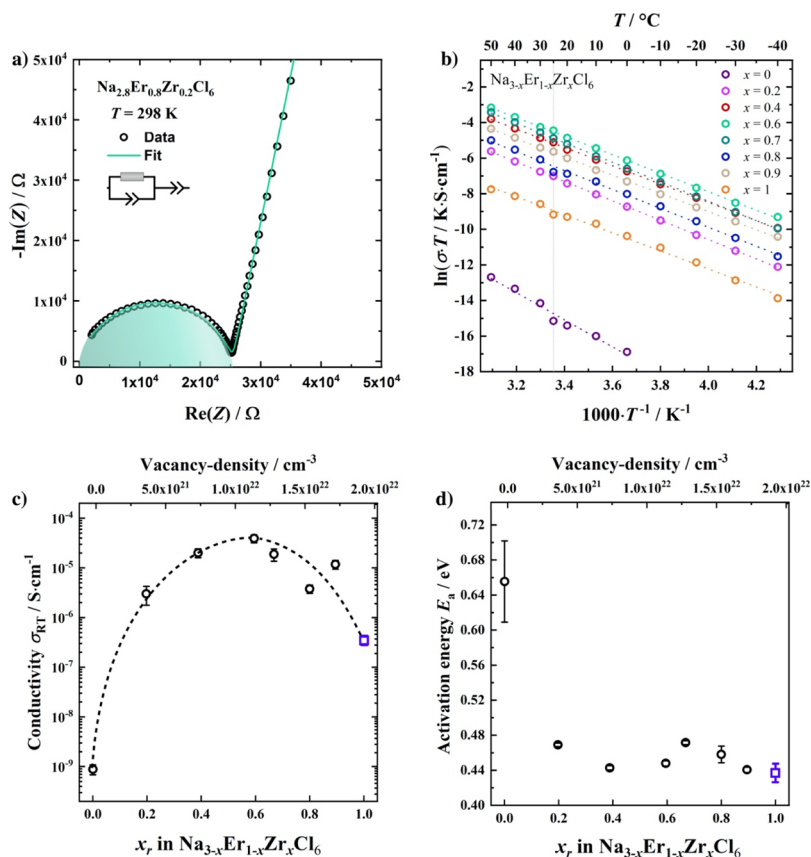


**Figure 7.** Representative Nyquist plot of a room-temperature impedance measurement (a) and Arrhenius plots from the temperature dependent measurements (b). The spectra of  $\text{Na}_3\text{ErCl}_6$  below  $0^\circ\text{C}$  cannot be resolved and are therefore excluded from the Arrhenius plot. Extracted ionic conductivities (c) and activation energies (d). A significant increase of the ionic conductivity, peaking around a substitution degree of  $x = 0.6$  is governed by a decreasing activation energy.

used to shed light on the landscape of the local coordination environment of the sodium ion. Figure 6a shows the obtained isosurface for a selected composition of  $\text{Na}_{2.8}\text{Er}_{0.8}\text{Zr}_{0.2}\text{Cl}_6$ , representing the pathway with a lowest valence mismatch and energy for sodium. Three different tetrahedral interstitial positions are possible which are found to be somewhat energetically stable by the bond-valence sums. Figure 6b represents the associated energy landscape with the corresponding pathways, as shown in 6c–e. As expected by the existence of mostly edge-sharing octahedra, the main pathways include these tetrahedral transition sites.

Three different pathways can be thought of (1) a direct pathway from the octahedral Na-position to the prismatic (red pathway) (Figure 6b,c) without involving any of these interstitial positions. (2) A less direct transition from an octahedron to a prism or *vice versa* through two of the interstitial transition sites (i1 and i2, green pathway, Figure 6b,d) and an octahedra–octahedra transition involving the third interstitial site i3 and the corresponding pathway in blue (Figure 6b,e). Although the interstitial sites appear to be energetically stable suggested by the bond valence sum calculations, no occupation of the respective sites could be verified using Rietveld refinements. Therefore, those interstitial sites are likely too short-lived as intermediate states for ionic diffusion and overall activation barriers between 0.4 and 0.6 eV can be expected in  $\text{Na}_{2.4}\text{Er}_{0.4}\text{Zr}_{0.6}\text{Cl}_6$ .

**3.5. Ionic Transport Properties.** Temperature-dependent impedance spectroscopy was used to access the influence of

the changing structural features on the transport properties. While Meyer *et al.* evaluated the temperature-dependent behavior of the structure,<sup>48</sup> no Na-ion transport properties are known for  $\text{Na}_3\text{ErCl}_6$ . Figure 7a shows a representative Nyquist plot of one of the collected room temperature impedance data sets ( $\text{Na}_{3-x}\text{Er}_{1-x}\text{Zr}_x\text{Cl}_6$  with  $x = 0.2$ ). The remaining Nyquist plots can be found in Supporting Information (Figure S3). A parallel resistor-constant phase element combination that is in series to a second constant phase element is used as the equivalent circuit (shown as inset of Figure 7a) for fitting the impedance data. The process corresponds to the bulk contribution ( $46\text{ pF}\cdot\text{cm}^{-2}$ ) and ion-blocking behavior of the used steel electrodes, respectively. As bulk and grain boundary contributions cannot be reasonably deconvoluted, even at low temperature up to  $-40^\circ\text{C}$ , the here reported conductivities represent total conductivities. The comparison of all obtained Arrhenius plots is shown in Figure 7b, and the extracted room-temperature conductivities and activation energies are shown in Figure 7c,d, respectively.

The ionic conductivity of the pristine  $\text{Na}_3\text{ErCl}_6$  of  $10^{-6}\text{ mS}\cdot\text{cm}^{-1}$  ( $25^\circ\text{C}$ ) can be attributed to the absence of vacant  $\text{Na}^+$  site in the structure. Upon  $\text{Zr}^{4+}$  introduction, the conductivity of  $\text{Na}_{3-x}\text{Er}_{1-x}\text{Zr}_x\text{Cl}_6$  increases and reaches a maximum value of  $0.035\text{ mS}\cdot\text{cm}^{-1}$  ( $25^\circ\text{C}$ ) for  $\text{Na}_{2.4}\text{Er}_{0.4}\text{Zr}_{0.6}\text{Cl}_6$ , followed by a strong decrease afterward that ends up at  $3.5\cdot 10^{-7}\text{ mS}\cdot\text{cm}^{-1}$  for  $\text{Na}_2\text{ZrCl}_6$ .

Together with the increasing conductivity, the activation barriers first decrease significantly. Although this seems

counter intuitive as the volume of the polyhedral pathways shrinks, it is likely associated with the introduction of vacancies here. Vacancy formation enthalpies play a large role in the activation barriers, and introduction of vacancies is often observed to decrease the activation barrier in Na<sup>+</sup> conductors such as Na<sub>3</sub>PS<sub>4</sub> and Na<sub>3</sub>SbS<sub>4</sub>.<sup>4,55</sup> Slight variations to the activation barriers can be found after a substitution degree of  $x = 0.6$ . It was not possible to relate these to any structural feature, including Na and Er/Zr polyhedra volumes, transition tetrahedra volumes, and transition areas. Possibly, a highly complex combination of charge carrier density, diffusion pathway, and local distortion is responsible for the observed behavior. Nevertheless, these changes are overall minor, considering the typical uncertainties for activation barriers.<sup>52</sup>

Overall, the introduction of vacancies leads to a tunable ionic conductivity in the series of solid solutions Na<sub>3-x</sub>Er<sub>1-x</sub>Zr<sub>x</sub>Cl<sub>6</sub>, which in turn provides a promising step toward halide-based sodium-ion conductors.

#### 4. CONCLUSIONS

In this paper, we report the discovery of the Na-ion-conducting chloride solid electrolyte Na<sub>3-x</sub>Er<sub>1-x</sub>Zr<sub>x</sub>Cl<sub>6</sub> together with a successful optimization of the ionic conductivity by aliovalent substitution. The introduction of the smaller Zr<sup>4+</sup>-ion leads to reduced lattice parameters along a series of solid solutions, with the only exception of the endmember Na<sub>2</sub>ZrCl<sub>6</sub> that crystallizes in a different space group. Interesting nonlinear structural changes were observed that can be linked to the polyhedral linkage of prisms and octahedra composing the structure, showing the interplay of structural motifs, polyhedral rotations, and polyhedral volumes during a substitution.

By introducing vacancies, the ionic conductivity increases to values of 0.035 mS·cm<sup>-1</sup> for Na<sub>2.4</sub>Er<sub>0.4</sub>Zr<sub>0.6</sub>Cl. While these values seem low when compared to the lithium counterparts of these halides, these novel compositions represent a promising first step in sodium halide-based sodium-ion conductors. Nevertheless, replacements for the expensive elements and studies on the electrochemical potential window, in conjunction with achieving higher ionic conductivities are clearly needed.

#### ■ ASSOCIATED CONTENT

##### Supporting Information

The Supporting Information is available free of charge at <https://pubs.acs.org/doi/10.1021/acsaem.0c01870>.

All Rietveld refinements against collected capillary diffraction data and corresponding fit parameters for every composition and Nyquist plots of all compositions (PDF)

#### ■ AUTHOR INFORMATION

##### Corresponding Author

Wolfgang G. Zeier – Institute for Inorganic and Analytical Chemistry, University of Muenster, 48149 Muenster, Germany; [orcid.org/0000-0001-7749-5089](https://orcid.org/0000-0001-7749-5089); Email: [wzeier@uni-muenster.de](mailto:wzeier@uni-muenster.de)

##### Authors

Roman Schlem – Institute for Inorganic and Analytical Chemistry, University of Muenster, 48149 Muenster, Germany  
Ananya Banik – Institute for Inorganic and Analytical Chemistry, University of Muenster, 48149 Muenster, Germany

Mirco Eckardt – Department of Chemistry, University of Bayreuth, D-95440 Bayreuth, Germany

Mirijam Zobel – Department of Chemistry, University of Bayreuth, D-95440 Bayreuth, Germany; [orcid.org/0000-0002-8207-8316](https://orcid.org/0000-0002-8207-8316)

Complete contact information is available at: <https://pubs.acs.org/doi/10.1021/acsaem.0c01870>

#### Notes

The authors declare no competing financial interest.

#### ■ ACKNOWLEDGMENTS

The research was supported by the Deutsche Forschungsgemeinschaft (DFG) under grant no. ZE 1010/4-1. A.B. acknowledges the Alexander von Humboldt Foundation for the financial support through a Postdoctoral Fellowship.

#### ■ REFERENCES

- (1) Goodenough, J. B.; Park, K.-S. The Li-Ion Rechargeable Battery: A Perspective. *J. Am. Chem. Soc.* **2013**, *135*, 1167–1176.
- (2) Janek, J.; Zeier, W. G. A Solid Future for Battery Development. *Nat. Energy* **2016**, *1*, 16141.
- (3) Zheng, F.; Kotobuki, M.; Song, S.; Lai, M. O.; Lu, L. Review on Solid Electrolytes for All-Solid-State Lithium-Ion Batteries. *J. Power Sources* **2018**, *389*, 198–213.
- (4) Fuchs, T.; Culver, S. P.; Till, P.; Zeier, W. G. Defect-Mediated Conductivity Enhancements in Na<sub>3-x</sub>Pn<sub>1-x</sub>W<sub>2</sub>S<sub>4</sub> (Pn = P, Sb) Using Aliovalent Substitutions. *ACS Energy Lett.* **2020**, *5*, 146–151.
- (5) Kraft, M. A.; Ohno, S.; Zinkevich, T.; Koerver, R.; Culver, S. P.; Fuchs, T.; Senyshyn, A.; Indris, S.; Morgan, B. J.; Zeier, W. G. Inducing High Ionic Conductivity in the Lithium Superionic Argyrodites Li<sub>6+x</sub>P<sub>1-x</sub>Ge<sub>x</sub>S<sub>5</sub>I for All-Solid-State Batteries. *J. Am. Chem. Soc.* **2018**, *140*, 16330–16339.
- (6) Kuhn, A.; Gerbig, O.; Zhu, C.; Falkenberg, F.; Maier, J.; Lotsch, B. V. A New Ultrafast Superionic Li-Conductor: Ion Dynamics in Li<sub>11</sub>Si<sub>2</sub>PS<sub>12</sub> and Comparison with Other Tetragonal LGPS-Type Electrolytes. *Phys. Chem. Chem. Phys.* **2014**, *16*, 14669–14674.
- (7) Kato, Y.; Hori, S.; Saito, T.; Suzuki, K.; Hirayama, M.; Mitsui, A.; Yonemura, M.; Iba, H.; Kanno, R. High-Power All-Solid-State Batteries Using Sulfide Superionic Conductors. *Nat. Energy* **2016**, *1*, 16030.
- (8) Culver, S. P.; Koerver, R.; Zeier, W. G.; Janek, J. On the Functionality of Coatings for Cathode Active Materials in Thiophosphate-Based All-Solid-State Batteries. *Adv. Energy Mater.* **2019**, *9*, 1900626.
- (9) Zhang, W.; Weber, D. A.; Weigand, H.; Arlt, T.; Manke, I.; Schröder, D.; Koerver, R.; Leichtweiß, T.; Hartmann, P.; Zeier, W. G.; Janek, J. Interfacial Processes and Influence of Composite Cathode Microstructure Controlling the Performance of All-Solid-State Lithium Batteries. *ACS Appl. Mater. Interfaces* **2017**, *9*, 17835–17845.
- (10) Koerver, R.; Aygün, I.; Leichtweiß, T.; Dietrich, C.; Zhang, W.; Binder, J. O.; Hartmann, P.; Zeier, W. G.; Janek, J. Capacity Fade in Solid-State Batteries: Interphase Formation and Chemomechanical Processes in Nickel-Rich Layered Oxide Cathodes and Lithium Thiophosphate Solid Electrolytes. *Chem. Mater.* **2017**, *29*, 5574–5582.
- (11) Barpanda, P.; Oyama, G.; Nishimura, S. I.; Chung, S. C.; Yamada, A. A 3.8-V Earth-Abundant Sodium Battery Electrode. *Nat. Commun.* **2014**, *5*, 4358.
- (12) Ellis, B. L.; Nazar, L. F. Sodium and Sodium-Ion Energy Storage Batteries. *Curr. Opin. Solid State Mater. Sci.* **2012**, *16*, 168–177.
- (13) Zhu, Z.; Chu, I.-H.; Deng, Z.; Ong, S. P. Role of Na<sup>+</sup> Interstitials and Dopants in Enhancing the Na<sup>+</sup> Conductivity of the Cubic Na<sub>3</sub>PS<sub>4</sub> Superionic Conductor. *Chem. Mater.* **2015**, *27*, 8318–8325.

- (14) Krauskopf, T.; Pompe, C.; Kraft, M. A.; Zeier, W. G. Influence of Lattice Dynamics on  $\text{Na}^+$  Transport in the Solid Electrolyte  $\text{Na}_3\text{PS}_{4-x}\text{Se}_x$ . *Chem. Mater.* **2017**, *29*, 8859–8869.
- (15) Krauskopf, T.; Muy, S.; Culver, S. P.; Ohno, S.; Delaire, O.; Shao-Horn, Y.; Zeier, W. G. Comparing the Descriptors for Investigating the Influence of Lattice Dynamics on Ionic Transport Using the Superionic Conductor  $\text{Na}_3\text{PS}_{4-x}\text{Se}_x$ . *J. Am. Chem. Soc.* **2018**, *140*, 14464–14473.
- (16) Zhang, Z.; Roy, P.-N.; Li, H.; Avdeev, M.; Nazar, L. F. Coupled Cation-Anion Dynamics Enhances Cation Mobility in Room-Temperature Superionic Solid-State Electrolytes. *J. Am. Chem. Soc.* **2019**, *141*, 19360–19372.
- (17) Duchardt, M.; Neuberger, S.; Ruschewitz, U.; Krauskopf, T.; Zeier, W. G.; Gu, D.; Adams, S.; Roling, B.; Dehnen, S. Superior Conductor  $\text{Na}_{11}\text{Sn}_2\text{IP}_0.9\text{Se}_{12}$ : Lowering the Activation Barrier of  $\text{Na}^+$  Conduction in Quaternary 1–4–5–6 Electrolytes. *Chem. Mater.* **2018**, *30*, 4134–4139.
- (18) Duchardt, M.; Ruschewitz, U.; Adams, S.; Dehnen, S.; Roling, B. Vacancy-Controlled  $\text{Na}^+$  Superion Conduction in  $\text{Na}_{11}\text{Sn}_2\text{PS}_{12}$ . *Angew. Chem., Int. Ed.* **2018**, *57*, 1351–1355.
- (19) Zhang, Z.; Ramos, E.; Lalère, F.; Assoud, A.; Kaup, K.; Hartman, P.; Nazar, L. F.  $\text{Na}_{11}\text{Sn}_2\text{PS}_{12}$ : A New Solid State Sodium Superionic Conductor. *Energy Environ. Sci.* **2018**, *11*, 87–93.
- (20) Kraft, M. A.; Gronych, L. M.; Famprikis, T.; Ohno, S.; Zeier, W. G. Structure and Sodium Ion Transport in  $\text{Na}_{11+x}\text{Sn}_{2+x}(\text{Sb}_{1-y}\text{P}_y)_{1-x}\text{S}_{12}$ . *Chem. Mater.* **2020**, *32*, 6566–6576.
- (21) Winand, J.-M.; Rulmont, A.; Tarte, P. Nouvelles Solutions Solides  $\text{L}(\text{M})_{2-x}(\text{N})_x(\text{PO}_4)_3$  (L = Li, Na, M, N = Ge, Sn, Ti, Zr, Hf) Synthèse et Etude Par Diffraction x et Conductivité Ionique. *J. Solid State Chem.* **1991**, *93*, 341–349.
- (22) Guin, M.; Tietz, F. Survey of the Transport Properties of Sodium Superionic Conductor Materials for Use in Sodium Batteries. *J. Power Sources* **2015**, *273*, 1056–1064.
- (23) Delmas, C.; Nadiri, A.; Soubeyroux, J. L. The Nasicon-Type Titanium Phosphates  $\text{ATi}_2(\text{PO}_4)_3$  (A = Li, Na) as Electrode Materials. *Solid State Ionics* **1988**, *28–30*, 419–423.
- (24) Schlem, R.; Till, P.; Weiss, M.; Krauskopf, T.; Culver, S. P.; Zeier, W. G. Ionic Conductivity of the NASICON-Related Thiophosphate  $\text{Na}_{1+x}\text{Ti}_{2-x}\text{Ga}_x(\text{PS}_4)_3$ . *Chem.—Eur. J.* **2019**, *25*, 4143–4148.
- (25) Fabry, P.; Gros, J. P.; Million-Brodaz, J. F.; Kleitz, M. Nasicon, an Ionic Conductor for Solid-State  $\text{Na}^+$ -Selective Electrode. *Sens. Actuators* **1988**, *15*, 33–49.
- (26) Hayashi, A.; Noi, K.; Sakuda, A.; Tatsumisago, M. Superionic Glass-Ceramic Electrolytes for Room-Temperature Rechargeable Sodium Batteries. *Nat. Commun.* **2012**, *3*, 856.
- (27) Manthiram, A.; Yu, X.; Wang, S. Lithium Battery Chemistries Enabled by Solid-State Electrolytes. *Nat. Rev. Mater.* **2017**, *2*, 16103.
- (28) Kato, Y.; Shiotani, S.; Morita, K.; Suzuki, K.; Hirayama, M.; Kanno, R. All-Solid-State Batteries with Thick Electrode Configurations. *J. Phys. Chem. Lett.* **2018**, *9*, 607–613.
- (29) Famprikis, T.; Canepa, P.; Dawson, J. A.; Islam, M. S.; Masquelier, C. Fundamentals of Inorganic Solid-State Electrolytes for Batteries. *Nat. Mater.* **2019**, *18*, 1278–1291.
- (30) Wang, Y.; Richards, W. D.; Ong, S. P.; Miara, L. J.; Kim, J. C.; Mo, Y.; Ceder, G. Design Principles for Solid-State Lithium Superionic Conductors. *Nat. Mater.* **2015**, *14*, 1026–1031.
- (31) Prasada Rao, R.; Chen, H.; Adams, S. Stable Lithium Ion Conducting Thiophosphate Solid Electrolytes  $\text{Li}_x(\text{PS}_4)_n\text{YX}_z$  (X = Cl, Br, I). *Chem. Mater.* **2019**, *31*, 8649–8662.
- (32) Anantharamulu, N.; Koteswara Rao, K.; Rambabu, G.; Vijaya Kumar, B.; Radha, V.; Vithal, M. A Wide-Ranging Review on Nasicon Type Materials. *J. Mater. Sci.* **2011**, *46*, 2821–2837.
- (33) Muy, S.; Voss, J.; Schlem, R.; Koerver, R.; Sedlmaier, S. J.; Maglia, F.; Lamp, P.; Zeier, W. G.; Shao-Horn, Y. High-Throughput Screening of Solid-State Li-Ion Conductors Using Lattice-Dynamics Descriptors. *iScience* **2019**, *16*, 270–282.
- (34) Schlem, R.; Bernges, T.; Li, C.; Kraft, M. A.; Minafra, N.; Zeier, W. G. A Lattice Dynamical Approach for Finding the Lithium Halide Superionic Conductor  $\text{Li}_3\text{ErI}_6$ . *ACS Appl. Energy Mater.* **2020**, *3*, 3684–3691.
- (35) Schlem, R.; Muy, S.; Prinz, N.; Banik, A.; Shao-Horn, Y.; Zobel, M.; Zeier, W. G. Mechanochemical Synthesis: A Tool to Tune Cation Site Disorder and Ionic Transport Properties of  $\text{Li}_3\text{MCl}_6$  (M = Y, Er) Superionic Conductors. *Adv. Energy Mater.* **2019**, *10*, 1903719.
- (36) Park, K.-H.; Kaup, K.; Assoud, A.; Zhang, Q.; Wu, X.; Nazar, L. F. High-Voltage Superionic Halide Solid Electrolytes for All-Solid-State Li-Ion Batteries. *ACS Energy Lett.* **2020**, *5*, 533–539.
- (37) Li, X.; Liang, J.; Luo, J.; Norouzi Banis, M.; Wang, C.; Li, W.; Deng, S.; Yu, C.; Zhao, F.; Hu, Y.; Sham, T.-K.; Zhang, L.; Zhao, S.; Lu, S.; Huang, H.; Li, R.; Adair, K. R.; Sun, X. Air-Stable  $\text{Li}_3\text{InCl}_6$  Electrolyte with High Voltage Compatibility for All-Solid-State Batteries. *Energy Environ. Sci.* **2019**, *12*, 2665–2671.
- (38) Li, X.; Liang, J.; Chen, N.; Luo, J.; Adair, K. R.; Wang, C.; Banis, M. N.; Sham, T. K.; Zhang, L.; Zhao, S.; Lu, S.; Huang, H.; Li, R.; Sun, X. Water-Mediated Synthesis of a Superionic Halide Solid Electrolyte. *Angew. Chem.* **2019**, *131*, 16579–16584.
- (39) Asano, T.; Sakai, A.; Ouchi, S.; Sakaida, M.; Miyazaki, A.; Hasegawa, S. Solid Halide Electrolytes with High Lithium-Ion Conductivity for Application in 4 V Class Bulk-Type All-Solid-State Batteries. *Adv. Mater.* **2018**, *30*, 1803075.
- (40) Wang, S.; Bai, Q.; Nolan, A. M.; Liu, Y.; Gong, S.; Sun, Q.; Mo, Y. Lithium Chlorides and Bromides as Promising Solid-State Chemistries for Fast Ion Conductors with Good Electrochemical Stability. *Angew. Chem., Int. Ed.* **2019**, *58*, 8039–8043.
- (41) Cheng, J.; Sivonxay, E.; Persson, K. A. Evaluation of Amorphous Oxide Coatings for High-Voltage Li-Ion Battery Applications Using a First-Principles Framework. *ACS Appl. Mater. Interfaces* **2020**, *12*, 35748–35756.
- (42) Qie, Y.; Wang, S.; Fu, S.; Xie, H.; Sun, Q.; Jena, P. Yttrium-Sodium Halides as Promising Solid-State Electrolytes with High Ionic Conductivity and Stability for Na-Ion Batteries. *J. Phys. Chem. Lett.* **2020**, *11*, 3376–3383.
- (43) Atkinson, A. W.; Chadwick, J. R.; Kinsella, E. Studies of Some Indium-Chlorine Compounds. *J. Inorg. Nucl. Chem.* **1968**, *30*, 401–408.
- (44) Thomae, S. L. J.; Prinz, N.; Hartmann, T.; Teck, M.; Correll, S.; Zobel, M. Pushing Data Quality for Laboratory Pair Distribution Function Experiments. *Rev. Sci. Instrum.* **2019**, *90*, 043905.
- (45) Adams, S. Bond Valence Analysis of Structure-Property Relationships in Solid Electrolytes. *J. Power Sources* **2006**, *159*, 200–204.
- (46) Seifert, H. J. Ternary Chlorides of the Trivalent Late Lanthanides: Phase Diagrams, Crystal Structures and Thermodynamic Properties. *J. Therm. Anal. Calorim.* **2006**, *83*, 479–505.
- (47) Steiner, H.-J.; Lutz, H. D. Neue Schnelle Ionenleiter Vom Typ  $\text{MI}_3\text{MIIICl}_6$  (MI = Li, Na, Ag; MIII = In, Y). *ZAAC - J. Inorg. Gen. Chem.* **1992**, *613*, 26–30.
- (48) Meyer, G.; Peter Ax, S.; Schleid, T.; Irmeler, M. The Chlorides  $\text{Na}_3\text{MCl}_6$  (M = Eu, Lu, Y, Sc): Synthesis, Crystal Structures, and Thermal Behaviour. *Z. Anorg. Allg. Chem.* **1987**, *554*, 25–33.
- (49) Culver, S. P.; Koerver, R.; Krauskopf, T.; Zeier, W. G. Designing Ionic Conductors: The Interplay between Structural Phenomena and Interfaces in Thiophosphate-Based Solid-State Batteries. *Chem. Mater.* **2018**, *30*, 4179–4192.
- (50) Shannon, R. D. Revised Effective Ionic Radii and Systematic Studies of Interatomic Distances in Halides and Chalcogenides. *Acta Crystallogr., Sect. A: Cryst. Phys., Diffr., Theor. Gen. Crystallogr.* **1976**, *32*, 751.
- (51) Xu, Z.; Chen, X.; Liu, K.; Chen, R.; Zeng, X.; Zhu, H. Influence of Anion Charge on Li Ion Diffusion in a New Solid-State Electrolyte,  $\text{Li}_3\text{LaI}_6$ . *Chem. Mater.* **2019**, *31*, 7425–7433.
- (52) Ohno, S.; Bernges, T.; Buchheim, J.; Duchardt, M.; Hatz, A.-K.; Kraft, M. A.; Kwak, H.; Santhosha, A. L.; Liu, Z.; Minafra, N.; Tsuji, F.; Sakuda, A.; Schlem, R.; Xiong, S.; Zhang, Z.; Adelhelm, P.; Chen, H.; Hayashi, A.; Jung, Y. S.; Lotsch, B. V.; Roling, B.; Vargas-Barbosa, N. M.; Zeier, W. G. How Certain Are the Reported Ionic

Conductivities of Thiophosphate-Based Solid Electrolytes? An Interlaboratory Study. *ACS Energy Lett.* **2020**, *5*, 910–915.

(53) Schlem, R.; Ghidui, M.; Culver, S. P.; Hansen, A.-L.; Zeier, W. G. Changing the Static and Dynamic Lattice Effects for the Improvement of the Ionic Transport Properties within the Argyrodite  $\text{Li}_6\text{PS}_{5-x}\text{Se}_x\text{I}$ . *ACS Appl. Energy Mater.* **2020**, *3*, 9–18.

(54) Krauskopf, T.; Culver, S. P.; Zeier, W. G. Bottleneck of Diffusion and Inductive Effects in  $\text{Li}_{10}\text{Ge}_{1-x}\text{Sn}_x\text{P}_2\text{S}_{12}$ . *Chem. Mater.* **2018**, *30*, 1791–1798.

(55) Bo, S.-H.; Wang, Y.; Kim, J. C.; Richards, W. D.; Ceder, G. Computational and Experimental Investigations of Na-Ion Conduction in Cubic  $\text{Na}_3\text{PSe}_4$ . *Chem. Mater.* **2016**, *28*, 252–258.